

Grapevine buds detection and localization in 3D space based on Structure from Motion and 2D image classification

Carlos Ariel Díaz^{a,*}, Diego Sebastián Pérez^b, Humberto Miatello^c, Facundo Bromberg^b

^a*Universidad Tecnológica Nacional, Facultad Regional Mendoza, Laboratorio de Inteligencia Artificial DHARMa, Dpto. de Sistemas de la Información. Rodríguez 273, CP 5500, Mendoza, Argentina.*

^b*Universidad Tecnológica Nacional, Facultad Regional Mendoza, CONICET, Laboratorio de Inteligencia Artificial DHARMa, Dpto. de Sistemas de la Información. Rodríguez 273, CP 5500, Mendoza, Argentina.*

^c*iNOSUR LLC, New Lab, 19 Morris Ave, New York, Brooklyn, NY 11205, New York, United States.*

Abstract

In viticulture, there are several applications where 3D bud detection and localization in vineyards is a necessary task susceptible to automation: measurement of sunlight exposure, autonomous pruning, bud counting, type-of-bud classification, bud geometric characterization, internode length, and bud development stage. This paper presents a workflow to achieve quality 3D localizations of grapevine buds based on well-known computer vision and machine learning algorithms when provided with images captured in natural field conditions (i.e., natural sunlight and the addition of no artificial elements), during the winter season and using a mobile phone RGB camera. Our pipeline combines the Oriented FAST and Rotated BRIEF (ORB) for keypoint detection, a Fast Local Descriptor for Dense Matching (DAISY) for describing the keypoint, and the Fast Approximate Nearest Neighbor (FLANN) technique for matching keypoints, with the Structure from Motion multi-view scheme for generating consistent 3D point clouds. Next, it uses a 2D scanning window classifier based

*Corresponding author

Email addresses: `carlos.diaz@frm.utn.edu.ar` (Carlos Ariel Díaz), `sebastian.perez@frm.utn.edu.ar` (Diego Sebastián Pérez), `humberto.m@inosur.com` (Humberto Miatello), `fbromberg@frm.utn.edu.ar` (Facundo Bromberg)

on Bag of Features and Support Vectors Machine for classification of 3D points in the cloud. Finally, the Density-Based Spatial Clustering of Applications with Noise (DBSCAN) for 3D bud localization is applied. Our approach resulted in a maximum *precision* of 1.0 (i.e., no false detections), a maximum *recall* of 0.45 (i.e. 45% of the buds detected), and a localization error within the range of 259 – 554 pixels (corresponding to approximately 3 bud diameters, or 1.5cm) when evaluated over the whole range of user-given parameters of workflow components.

Keywords: Computer vision, Grapevine bud detection, Precision viticulture

1. Introduction

In this work, we present an approach for the efficient 3D detection and localization of grapevine buds. 3D models were reconstructed from multiple images captured during the winter season in natural field conditions (i.e., natural sunlight and the addition of no artificial elements) using a mobile phone RGB camera.

Grapevine buds were recognized early in viticulture history as one of the most important parts of the plant, mainly because they contain the whole plant productive capacity, from which all sprouts, leaves, bunches, and tendrils grow. In particular, bud bunch fertility, a.k.a. *fruitfulness*, is of particular interest, as it has a direct impact on the main goal of vine production, that is, to increase productivity without affecting fruit quality. It has been shown that bud fruitfulness depends on the amount of sunlight exposure of buds during the period starting at bud initiation in early spring throughout its development stage up to 30 days after bloom [15, 21, 11, 25, 35, 27]. Shading conditions during this period strongly depend on what we call *shading structure*, consisting in the localization and geometric characterization of those parts of the plant that occlude sunlight, mainly the leaves and bunches that grow after bloom. In addition, sunlight exposure can be used by growers to influence the productivity of the next period by choosing those buds that received the most sunlight exposure.

21 In practice, this happens by deciding pruning procedures late in the winter [23].
22 There is a balance, however, as unpruned buds will produce vegetation, shading
23 the newly initiated buds, and therefore, affecting the productivity of the next
24 period. The decision of optimal pruning is, therefore, a complex task that must
25 be carefully balanced between: (i) productivity maximization of the starting
26 period determined by buds with maximum sun exposure, and (ii) productiv-
27 ity maximization of the following period determined by the shading conditions
28 resulting from the green vegetation growing from those buds.

29 A solution to the first issue requires measuring the sun exposure of individ-
30 ual buds at regular intervals from initiation to 30 days after bloom and then
31 recovering this value for each bud months later during winter pruning. Sunlight
32 exposure has been measured so far through manual positioning of radiation
33 sensors [25]. These manual procedures, however, are far from efficient for the
34 massive measuring of sunlight exposure of individual plants, not to mention
35 of individual buds. Our work aims to partially fulfill the need for an efficient
36 method for measuring and recording the sunlight exposure of individual buds.
37 The general rationale behind our approach is that it is possible to compute
38 the sunlight exposure of a bud with high-precision when the precise 3D local-
39 ization of the bud, the shading structure around it, the geo-positioning of the
40 field, and the dates of interest are fed to a sun radiation model [29, 8]. It is
41 an ambitious goal, attended partially by the present work that provides a so-
42 lution to the 3D localization of winter buds. Future work, however, will have
43 to solve the problem of producing the shading model. This could be done by
44 localizing buds from initiation till the end of summer, and then by identifying
45 buds between consecutive 3D modelizations to allow the recording of long-term
46 sun exposure. A solution to the second issue requires a thorough understand-
47 ing of which summer shading structures result from different winter pruning
48 procedures and trellis systems [11, 14]. This demands measuring the shading
49 structure, a procedure which is currently unavailable.

50 Simulations are a possibility for partially overcoming the inability to recon-
51 struct the shading structure, necessary for solving both issues. There is a line of

52 research that studies different procedures for producing *simulated* whole plant
53 shading structures, including the canopy and bunches [13, 16]. They typically
54 require plant architecture and bud localization as input. However, bud local-
55 ization information, being inexistent, is provided by randomly simulating their
56 position. Our work provides a solution to the latter, while [26] is one of the
57 many studies that provide a solution to the former. Despite being a simulated
58 model, the shading structure has the potential to produce invaluable —and to
59 this day inexistent— information on the (simulated) long-term sun exposure of
60 large bud samples, including months with a fully grown canopy. In particular,
61 with plant architecture before the winter pruning, it is possible to simulate the
62 *backward* shading structure of the previous spring as well as different *forward*
63 shading structures resulting from different pruning treatments.

64 Finally, we note that both issues require an autonomous system for executing
65 pruning. Historically, pruning procedures have been simplified to be accessible
66 for humans. However, this may change with the extra information provided
67 by 3D modeling, namely, the identification of fruitful buds and predictions of
68 next-period’s shading structures. With this information, the resulting optimal
69 pruning may be too sophisticated to be amenable for human execution, requiring
70 autonomous pruning systems.

71 In addition to measuring sunlight exposure and guiding autonomous prun-
72 ing, bud localization is also required as part of the measuring processes of other
73 variables of interest in viticulture. These are bud count, type-of-bud classifi-
74 cation, bud geometric characterization, internode length, and bud development
75 stage. Their values at any location are of importance to agronomists for decid-
76 ing on possible treatments (e.g., the application of fertilizers, canopy pruning),
77 or for predicting plant productivity. Observation and measurement of crop vari-
78 ables is a fundamental task that offers the agronomist information about crop
79 state, providing the means for informed decision-making of what treatments
80 must be applied in order to maximize productivity and crop quality. At present,
81 these variables are measured through direct or indirect human visual inspection,
82 whose elevated cost often results in the measurement of only a small sample of

83 all cases. When data are scarce, even powerful statistical techniques may still
84 result in high uncertainty in the decision-making process, motivating the intro-
85 duction of improved sensing procedures. Locating buds is a necessary task to
86 conduct a proper measurement of the above variables. However, 2D localization
87 is sufficient for all variables with the exception of internode length, for which 3D
88 localization of two consecutive buds in a cane is necessary to avoid perspective
89 errors. Still, automatic, high-throughput measurement of these variables would
90 come with no extra cost with an autonomous 3D localization system in place.

91 *1.1. Related work*

92 There are many computational approaches to aid viticulture, including de-
93 tecting grapes and bunches, estimating grape size and weight, estimating pro-
94 duction and foliar area indexes, phenotyping, and autonomous selective pulver-
95 ization [19, 30, 6, 12, 2, 31]. For a more extensive review, see [37].

96 Specifically concerning the detection of grapevine buds, there are two re-
97 cent studies (in 2D only) that address the problem of grapevine bud detection
98 [38, 12]. The first one presents a grapevine bud detection algorithm designed
99 specifically to establish the groundwork for a future autonomous pruning sys-
100 tem in the winter season (with no leaves left that may occlude the vision and
101 operation of the cutting mechanism). Bud detection is performed from RGB
102 images (the image resolution in this study is unknown). Furthermore, on top of
103 this assumption, images are captured indoors with an industrial CCD camera
104 with controlled background and lighting conditions. To discriminate between
105 plant and background pixels, the authors apply a simple threshold resulting in a
106 binary image to obtain a wire skeleton of the plant. Under the assumption that
107 bud morphology is similar to that of the corners, they apply Harris' algorithm
108 [9] to the skeleton image for detecting those corners. This process produces a
109 recall of 0.702, i.e., 70.2% of buds detected. Although some improvements are
110 suggested by the authors, the most striking limitations of this work are the need
111 for images captured under controlled indoors conditions and the fact that the
112 resulting localizations are in 2D. A second work for bud detection is presented

113 by Herzog et al. [12]. This work introduces three methods of bud detection.
114 The best results are obtained with the semi-automatic method that requires
115 human intervention for validating the quality of the results. Detection is based
116 on 3456×2304 RGB images, where the scene is altered with an artificial black
117 background, producing a recall of 0.94. The authors argue that this recall is
118 enough to satisfy the phenotyping of plants. However, as the authors themselves
119 point out, these good results are mainly explained by the particular color and
120 morphology of the buds, captured when bud sprouts are visibly green and their
121 average size is around 2cm (compared to a typical 5mm diameter of a dormant
122 bud) which makes it easier to discriminate them visually from other plant com-
123 ponents. Although these works represent important advancements in specific
124 bud detection applications, they suffer from some of the following limitations:
125 (i) the use of an artificial background, (ii) controlled indoors luminosity, (iii) the
126 need for human intervention, (iv) the detection of buds in an advanced stage of
127 development, (v) detection is in 2D.

128 Dey et al. [5] introduced a pipeline for recovering the 3D structure of the
129 grapevine plant in the spring-summer season (i.e., with leaves and fruits) from
130 a 3D point cloud. This 3D point cloud visually represents the surface parts of
131 the environment, where each point is represented by a tuple containing the 3D
132 position in world coordinates (x, y, z) . Cloud reconstruction is obtained with
133 the algorithm proposed by Snavely et al. [28]. Afterwards, the cloud is classified
134 into leaves, branches, and fruits by means of a supervised classification algorithm
135 that uses shape and color features. The experiments show an accuracy of 0.98
136 for grapes before maturation (still green) and 0.96 for fully ripe grapes (color
137 change), where accuracy corresponds to the proportion of all observations (both
138 grapes and background) that were correctly classified. Despite the similarities
139 with our work, their work classifies grapes and ours classifies buds, making it
140 hard to compare them. This is mainly due to the geometrical nature of the
141 features they use that one would expect to work better for close-to-spherical
142 shapes such as that of grapes, but which may work poorly for buds that present
143 a highly irregular shape.

144 2. Materials and Methods

145 In this section we provide a detailed description of our approach of 3D de-
146 tection and localization of grapevine buds together with a detailed description
147 of the input collection of images.

148 The detection and localization workflow consists of five stages as depicted
149 in Fig.1: (1) a 3D construction technique known as *Structure from Motion* [10]
150 that, given as input a set of 2D images of some scene, produces both the 3D
151 geometry (point cloud) of the scene and the camera pose of each 2D image;
152 (2) a *scanning-window* technique [36] over each 2D image of the scene, used for
153 classifying each of the image-patches corresponding to each window as either a
154 bud or not, through the classifier presented by [20]; (3) a voting scheme for the
155 classification of each 3D point in the cloud as being part of a bud or not, based
156 on the number of patches and number of images in the scene that contain its
157 projection; (4) a clustering stage for the 3D detection of buds by running the
158 *DBSCAN* spatial clustering algorithm [7] over the 3D cloud points classified as
159 part of a bud, with each cluster representing a detected bud; (5) localization of
160 buds as the center of mass of the point cloud corresponding to each cluster.

161 The first stage consists in the use of the 3D reconstruction technique known
162 as *Structure from Motion (SfM)* [10] that, given as input a set of 2D images
163 of some scene, produces both the 3D geometry (point cloud) of the scene and
164 the camera pose of each 2D image (see an illustrative result of stage 1 in Fig.1,
165 corresponding to an actual scene reconstruction from images in the collection).
166 The method starts by detecting the keypoints of the 2D images using the *ORB*
167 (*Oriented FAST and Rotated BRIEF*) algorithm [24]. These keypoints are then
168 grouped in projection bundles, one per 3D point in the cloud, with each image
169 contributing at best one keypoint to the bundle. Each of the bundle keypoints
170 corresponds to the projection of the 3D point in its corresponding image. The
171 trick is that it is possible to construct these projection bundles before knowing
172 the actual location of the corresponding 3D point, by considering that keypoints
173 are the projection of the same 3D point if they match visually. This matching

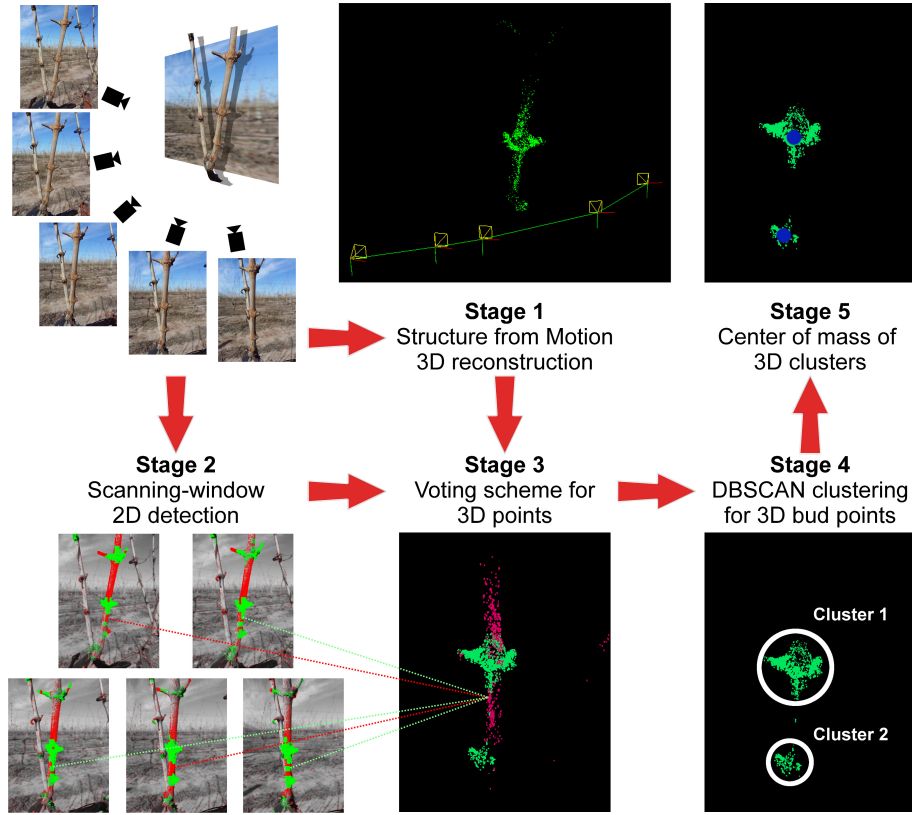


Figure 1: Schematics of the workflow for 3D bud detection and localization. The input is a set of 2D images of some scene (upper-left). Stage 1: estimation of 3D points and camera pose (cones) for 3D scene reconstruction by *Structure from Motion*. Stage 2: scanning-window 2D detection of buds over each 2D image of the scene, showing in green those keypoints classified as bud, and in red, those classified as non-bud. Stage 3: voting scheme to produce the classification of 3D points as bud or not (green and red dots, respectively). Stage 4: spatial clustering of all 3D bud points to individualize buds, by considering different clusters as different buds (white circles). Stage 5: locates buds as the center of mass of 3D points of clusters (blue dots for each cluster). (For interpretation of the references to color in this figure legend, the reader is referred to the web version of the article.)

174 is conducted by first applying the *DAISY* algorithm [32] to compute a visual
175 feature descriptor of the local neighborhood of each keypoint, and then using
176 the *FLANN* (*Fast Approximate Nearest Neighbor Search*) algorithm [18] to vi-
177 sually match keypoints of different images in the scene. To do this, it takes
178 every two images of the scene and performs a symmetric distance comparison,
179 in feature space, between the feature descriptors of their keypoints. More pre-
180 cisely, it considers that a keypoint k of the first image visually matches some
181 keypoint descriptor k' in the other, if on the one hand, it holds that among all
182 keypoints in the second image, descriptor k' is the closest to descriptor k . On
183 the other hand, the opposite also holds, that is, if among all descriptors in the
184 first image, descriptor k is the closest to descriptor k' . Ultimately, the goal is
185 to use these bundles to determine not only the position of these 3D points, but
186 also the camera pose of each image. Clearly, a single bundle is not enough, and
187 since it provides at most one projected point per image, it is insufficient to con-
188 strain its pose. Instead, more bundles increase the constraint, as they provide
189 more projected points per image, to eventually restrict its pose completely. In
190 practice, the matching is noisy, and there is no analytical solution to this con-
191 straint problem, so the process proceeds through a minimization called *bundle*
192 *adjustment* [33]. The bundle adjustment proceeds iteratively in an online mini-
193 mization process, proposing at each step a value for the camera pose parameters
194 as well as the coordinates of the 3D points and computes as cost function the
195 so called *reprojection error*. This is computed as follows: (i) first it uses the
196 camera poses to project each 3D point into each 2D image; (ii) then it computes
197 the squared distance between each keypoint in the image to its corresponding
198 projected position; and (iii) it sums these squared distance over all keypoints of
199 all 2D images and reports its squared root, resulting in a quantity measured in
200 pixel units. The implementation of SfM used in this work is that provided by
201 the OpenCV 3.2.0 open source library [3], which implements the SfM version¹ of
202 Hartley and Zisserman [10] described in this section. It also uses the third-party

¹http://docs.opencv.org/trunk/d4/d18/tutorial_sfm_scene_reconstruction.html

203 library *Ceres-Solver (A Nonlinear Least Squares Minimizer)* [1] for the bundle
204 adjustment minimization process.

205 The second stage of the proposed workflow runs a scanning-window 2D de-
206 tection technique [36] over each 2D image of the scene. This technique proceeds
207 by sliding a fixed size window over the whole image, at fixed size steps with
208 some overlap, and by classifying each image patch covered by each window ei-
209 ther containing a bud or not. The classification is performed using the classifier
210 proposed by [20]. The results are patches with known geometry and localiza-
211 tion in the image, classified either containing a bud or not. Results of this stage
212 are shown in stage 2 of Fig.1, with keypoints belonging to patches classified
213 as bud depicted in green (light gray) points, and those belonging to non-bud
214 patches depicted in red (dark gray). The classifier of Perez et al. proceeds in
215 a workflow of computer vision and machine learning sub-processes: (i) First,
216 it runs *Scale-Invariant Features Transform (SIFT)* [17] for computing the low-
217 level visual features of the keypoints of each patch; (ii) it then runs *Bag of*
218 *Features (BoF)* [4] for constructing a higher level descriptor of the patch, based
219 on patch keypoints and their SIFT descriptors; and (iii) it concludes by running
220 a *Support Vectors Machine* [34] modeler for training a binary classifier based
221 on a collection of labeled patches represented by their BoF descriptors. It is
222 important to note that in this work, we reproduced the same classifier of Perez
223 et al. by training with the parameters provided in their work and the training
224 collection made publicly available², leaving only the choice of scanning-windows
225 parameters, i.e., window size and step. At first glance, it would seem that in
226 order to obtain a good classification, one should choose a window and step sizes
227 so that each bud in the image is perfectly circumscribed by some patch. This is
228 clearly not only impossible to perform for all buds and images for fixed window
229 and step sizes of the training collection —as buds are variable in size— but
230 it is also impossible for a testing collection, since here bud sizes and positions
231 would be unknown. However, together with the classifier, Perez et. al. provide

²Available in <http://dharma.frm.utn.edu.ar/vise/bc/>

232 a robustness analysis for window geometry showing that the classifier is robust
233 to patches that have lost up to 40% of the bud’s pixels (i.e., at least 60% of the
234 bud’s pixels are visible), and it contains non-bud visual information covering up
235 to 80% of the patch (i.e., bud pixels cover at least 20% of the patch). Based on
236 these numbers and an approximate bud diameter of 150 pixels obtained from an
237 inspection of our collection of 2D images (see below for more details of this col-
238 lection), we chose a window size of 150×150 pixels and a step of 75 pixels. This
239 guarantees a 50% overlap between contiguous patches, considering that these
240 values should produce bud coverage within the accepted values of the robustness
241 analysis.

242 The third stage of the workflow combines the results of the first two stages:
243 the 3D position of keypoints and classification of patches to produce the classifi-
244 cation of these 3D points as part of a bud or not. The 3D classification proceeds
245 through a voting scheme for each 3D point that classifies it as being part of a
246 bud whenever the number of images in which it has been detected surpasses
247 a threshold τ_I . Here, a 3D point is considered as detected in some 2D image
248 whenever the keypoint in the projected bundle of this 3D point corresponding
249 to that image falls within a minimum number τ_P of bud patches of that image
250 (see Fig.1). The basic rationale behind this voting scheme is the intuition that
251 only true bud visual aspects will show in all images, whereas noisy detections
252 would show them in only one of the images and cancel them out by the voting
253 filter as long as it is kept in low levels. As with previous stages, this process
254 is illustrated in Fig.1, showing five lines going from one keypoint in each 2D
255 image in stage 2 to one 3D point in the reconstructed scene of stage 3. The
256 keypoints at the point of origin of these 5 lines correspond to a bundle, with 3
257 (2) of them classified as bud (no-bud), so both the keypoint and its line were
258 colored green (red), or light (dark) gray for grayscale versions of the image. As
259 seen in the image, the 3D point is colored red (dark gray), corresponding to
260 no-bud, a result of the voting scheme for threshold $\tau_I = 4$ or $\tau_I = 5$.

261 At this point we have a 3D point cloud, with each point in the cloud clas-
262 sified as being part of a bud or not. This however does not individualize buds,

263 nor does it provide a localization for them (a process conducted in the last two
264 stages of our workflow) also depicted in Fig.1. To do this, the workflow continues
265 with stage 4 that executes the *Density-Based Spatial Clustering of Applications*
266 *with Noise (DBSCAN)* [7] to spatially cluster the 3D bud points, considering
267 different clusters as different buds. This algorithm works under the fundamental
268 assumption that points located in dense regions belong to the same cluster, thus
269 searching for high density regions separated by low density regions. An impor-
270 tant property of this algorithm is that it requires no predetermination of the
271 number of clusters, a property necessary to automatize detection in scenes with
272 an a priori unknown number of buds. It is also designed to discover arbitrary-
273 shaped clusters and is robust to noisy points excluding them from any cluster.
274 The key idea of the cluster recognition process is to detect high density regions
275 by requiring for each point of a cluster that the region of radius r around it con-
276 tain at least m other points belonging to the same cluster. The two parameters r
277 and m are user-specified and may drastically affect the outcome of this stage (as
278 shown later in the results section 3). To conclude we have to deal with a rather
279 technical issue, necessary for a proper reproducibility of our workflow. Scene
280 reconstruction by the SfM method may result in rather arbitrary scales, with
281 differences of orders of magnitude, resulting in parameter values r which greatly
282 affect the DBSCAN process. To give a sense of this variation, we computed for
283 each scene the *mean minimum distance (MMD)* that reports the mean value of
284 the distance of each 3D point in the cloud of that scene to its closest 3D point
285 in the same scene. Fig.2 shows a histogram for MMD over the 47 scenes, in log
286 scale, showing a variation range of over 15 orders of magnitude. To address this
287 dispersion, we re-scaled the radius parameter r multiplying it by the MMD of
288 the scene before passing it to DBSCAN.

289 The workflow then ends with a fifth and final stage that locates buds in the
290 centers of mass of the 3D points of its cluster.

291 The final outcome of the workflow just described is bud clusters in 3D to-
292 gether with their respective centers of mass. An ideal correct outcome would,
293 therefore, consist of a number of clusters matching exactly the number of buds

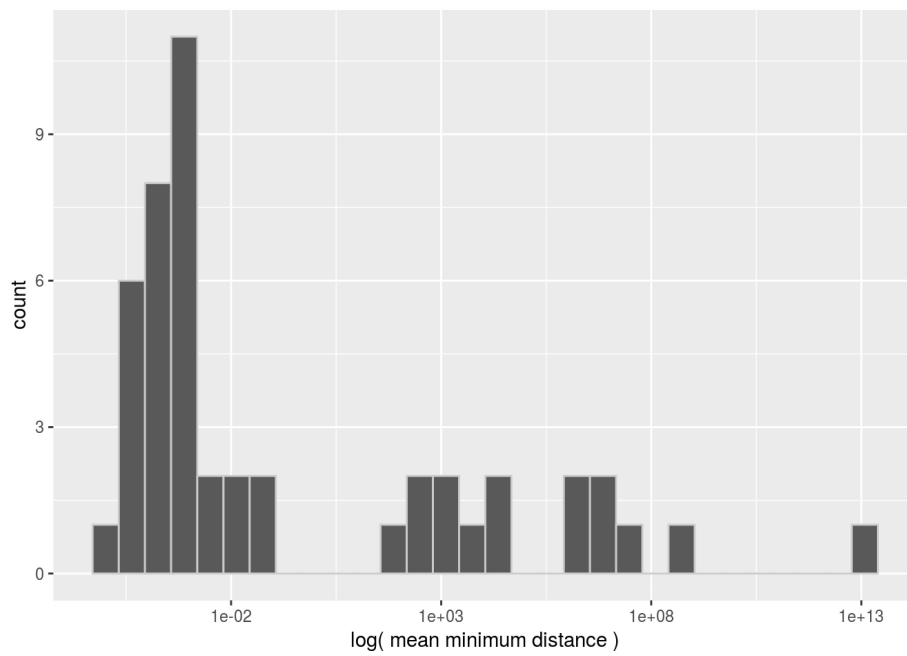


Figure 2: Histogram of the *mean minimum distance (MMD)* over the 47 scenes of the corpus, with the X-axis shown in log scale. The histogram shows the enormous dispersion in MMD, with cases ranging over 15 orders of magnitude.

294 in the scene, with their centers of mass coincident with the center of mass of
295 the buds. Instead, wrong outcomes would consist of mislocated clusters, worse,
296 spurious clusters, that correspond to no actual bud of the scene or buds that
297 have no cluster representing them. In the next subsection we describe in de-
298 tail the collection of 47 scenes used in the evaluation described in the following
299 section. It first introduces formally some performance measures that quantify
300 these different aspects of the quality of the 3D bud detection workflow. Then,
301 it reports their values for a representative spectrum of values for the four user-
302 defined parameters that control these outcomes (i.e., image-voting threshold τ_I ,
303 patch-voting threshold τ_P , DBSCAN radius r , DBSCAN minPts m).

304 *2.1. Collection of scenes and their 2D images*

305 We captured a collection of images that satisfy the requirements of this work:
306 they were taken in the winter season using RGB mobile phone cameras in natural
307 field conditions. In addition, there are specific requirements for capturing 2D
308 images imposed by the third-party modules of the proposed workflow: the SfM
309 module of OpenCV 3.2.0 for 3D reconstruction of grapevine branches and the
310 2D detection algorithm based on the approach of Perez et. al. [20]. Firstly, the
311 documentation of the SfM algorithm³ recommends in the order of 3-5 images for
312 a proper reconstruction, captured from differing points of view, but as close as
313 possible to one another. In addition, the elements of the scene (i.e., branches)
314 need to be well focused, and exposition levels kept within reasonable values.
315 Secondly, the scanning windows algorithm and the bud classifier used within
316 require buds of at least 100 pixels to maintain the robustness of classification
317 results, as recommended by the authors. This resulted in the following image
318 captured:

- 319 1. with a Samsung Galaxy A5 mobile phone camera, without flash, in JPEG
320 format, and a resolution of 4128×3096 pixels;

³http://docs.opencv.org/trunk/da/db5/group__reconstruction.html



Figure 3: Example of the images of one scene of the corpus, with circles marking the bud location.

- 321 2. satisfying the focus and exposition level requirements of the SfM modules
- 322 as detailed above, with 5 images per scene;
- 323 3. positioning the camera over an imaginary circular path around the branch,
- 324 at approximately equal displacements between them, with an overlap
- 325 above 80%, and always pointing toward the branch, conditions that guar-
- 326 antee a good reconstruction;
- 327 4. at a distance of 12cm from the branches to guarantee that buds are at
- 328 least 100 pixels in diameter for the chosen resolution;
- 329 5. on sunny days, under normal field conditions, without altering the scene
- 330 with artificial elements, and maintaining natural lighting conditions;
- 331 6. between 15:00 and 17:00 hours in late August (winter in the southern
- 332 hemisphere), when leaves are either dry or have fallen, but before sprouting
- 333 again (see Fig.3).

334 We captured 60 scenes for a total of 300 2D images, corresponding to branch

335 parts of a single grapevine plant (as exemplified by the 5 images of Fig.3). It

336 is worth mentioning that our workflow omits any automation for the selection

337 of input images in order to guarantee the success of the 3D reconstruction.

338 Therefore, from a total of 60 scenes, 10 were manually discarded for not following

339 the focus and exposition quality requirements of the SfM module. After the SfM

340 reconstruction, 3 more were discarded due to failure in reconstruction (detected

341 by reprojection errors of 60 pixels or more). After this manual pruning, the

342 collection was left with 235 images corresponding to the 47 remaining scenes,

343 with mean and standard deviations of the reprojection error of 2.91 and 5.41
344 pixels, respectively. Among these scenes we counted a total of 106 buds, with
345 an average of 2.25 buds per scene.

346 We ran the 2D bud classification over this image collection to assess the merit
347 of the 2D bud classifier of [20] for stage 2, when pre-trained over the original
348 image collection. To assess classifier recall, i.e., the proportion of true buds it
349 could detect, we considered two different collections of patches representing true
350 buds. The first was a collection of perfectly-circumscribed patches extracted
351 from rectangles that perfectly circumscribe each bud in each image collection.
352 Second, we ran a scanning-window of 150×150 pixels and a step of 75 pixels
353 and collected all patches that overlapped a bud on at least one pixel. We also
354 assessed the precision classifier, i.e., the proportion of detected buds that were
355 indeed true buds. To do this, we considered the same scanning-window, but this
356 time collected the complement set, i.e., all patches that did not contain a single
357 bud pixel. After running the classifier over all these image patches, we obtained
358 a recall of 0.978 for the perfectly-circumscribed patches, a recall of 0.0596 for the
359 single pixel overlapping cases, and a precision of 0.0511 for the non-overlapping
360 patches. The latter is a result of the fact that from all $\approx 559K$ patches of the
361 scanning-window containing no buds, 15756 were incorrectly classified as buds,
362 i.e., were *false positives*, drastically reducing the proportion of *true positives*
363 over all those classified as buds.

364 **3. Experiments**

365 In this section we present results of systematic experiments that evaluate
366 the quality of the 3D structures produced by our approach. We first introduce
367 quantitative performance measures that assess *detection* and *localization errors*
368 that report *hard* errors of true buds that were undetected, or clusters that de-
369 tected no bud, and *soft* errors reporting how far the correctly detected buds
370 fell from the actual position of the buds they detected. Values for these perfor-
371 mance measures are reported systematically for a representative range of values

372 of user-input parameters, the two thresholds τ_I and τ_P of the voting scheme
373 (stage 4), the radius r , and minimum number of points m of the DBSCAN
374 clustering algorithm.

375 3.1. Performance Measures

376 Now, let us explain the details of the *detection* and *localization* errors.

377 **Detection error:** This measure represents the *hard* errors of true buds
378 that were undetected or clusters that detected no bud, reported by the well-
379 known *precision* and *recall* measures, respectively. These are formally defined as
380 $recall = \frac{TP}{TP+FN}$ and $precision = \frac{TP}{TP+FP}$, with TP , FP , and FN denoting *true*
381 *positives*, *false positives*, and *false negatives*, respectively [22]. These quantities
382 contrast the results of our 3D detection workflow with the ground truth obtained
383 from manual detection of buds, corresponding to the center of mass of the perfect
384 circumscription rectangles described in the collection section above (c.f. section
385 2.1).

386 Specifically in this work, we consider that a bud has been correctly detected
387 —that is, it is a TP— whenever it satisfies *symmetrical closeness* to some cluster
388 —i.e., this bud is the closest bud to its closest cluster— with closeness being
389 measured in Euclidean distance in pixels. This definition of TPs could result in
390 clusters far away from a bud being counted as its TP, as long as they satisfy
391 symmetrical closeness. In practice, however, our results show this is not the case,
392 as worst localization errors are around 600 pixels. Additionally we consider that
393 a bud has been missed —that is, it is a FN— when its closest cluster is itself
394 closer to some other bud, and that a cluster detects no bud —that is, it is a
395 FP— when it is not the closer cluster to its closest bud. The definitions of
396 these quantities are illustrated in Fig.4. Dotted rectangles A and B mark buds
397 manually circumscribed with their center of mass marked as a dot within it.
398 The blue (dark) dots 1, 2, and 3 within the dotted circles mark the projection
399 of the center of mass of three detected bud clusters. Since cluster 1 is the closest
400 to bud B , and at the same time, bud B is the closest bud to cluster 1, then,
401 cluster 1 is the TP of bud B . In addition, even though clusters 2 and 3 have

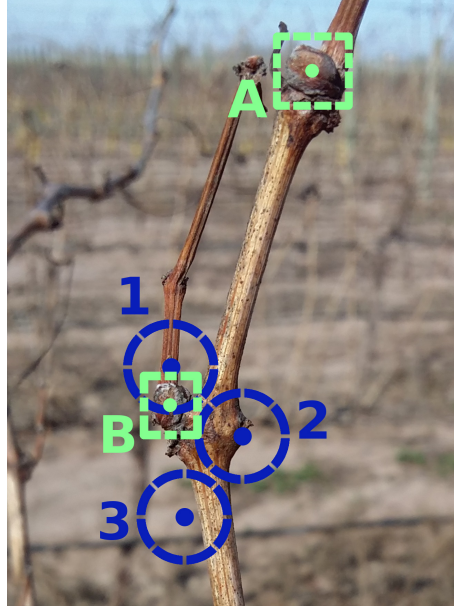


Figure 4: The figure illustrates the definitions of *true positives* (TP), *false positives* (FP), and *false negatives* (FN). Dotted rectangles *A* and *B* mark buds manually circumscribed with their centers of mass marked as a dot within it. The blue (dark) dots 1, 2, and 3 within the dotted circles mark the projection of the center of mass of three detected bud clusters whose position has been selected manually for illustration purposes. Since cluster 1 is the closest to bud *B*, and at the same time, bud *B* is the closest bud to cluster 1, then cluster 1 is the TP of bud *B*. Even though clusters 2 and 3 have bud *B* as the closest one, they are themselves not the closest to *B* (cluster 1 is), so they are FPs. Finally, bud *A* is a FN as none of the clusters has this bud as its closest. (For interpretation of the references to color in this figure legend, the reader is referred to the web version of the article.)

402 bud *B* as the closest one, they are themselves not the closest to *B* (cluster 1 is),
 403 so they are FPs. Finally, bud *A* is a false negative as none of the clusters has
 404 this bud as its closest.

405 **Localization error:** Detection error measured by precision and recall. It
 406 is an important measure of quality, but it may miss the *soft localization errors*
 407 that zoom into the detected buds represented by true positives and report how
 408 far their detection has fallen from their true position. Formally, we report as
 409 *localization error* the mean of the individual localization error of all buds, with

410 the individual localization error computed as the distance between the center
411 of mass of the circumscribed rectangle of the bud and the center of mass of its
412 symmetrically closest cluster.

413 The computation of precision, recall, and localization error require the 3D
414 coordinate of each bud’s center of mass. In practice, this demands measuring the
415 3D localization of each bud over a common coordinate system for all of them, an
416 extremely complex task to be performed manually, so the alternative of measur-
417 ing ground-truth 3D localizations for our collection was discarded as an option.
418 We considered instead an *approximated* alternative for measuring these errors,
419 one that computes them in the 2D pixel space of each image. Therefore, instead
420 of considering the 3D localizations of both clusters’ center of mass and bud’s
421 center of mass, it considers their *reprojected* localizations over each individual
422 image, i.e., their coordinates in the 2D pixel space of each image correspond-
423 ing to their position in the field of view of the camera corresponding to that
424 image. The computation of these reprojected localizations can be easily auto-
425 mated. Once computed, the computation of precision, recall and localization
426 errors followed exactly their 3D definition, but over 2D localizations, replacing
427 3D Euclidean distance with 2D Euclidean distance in pixels. Fig.5 illustrates
428 this approximation with the image on the right showing two clusters of the 3D
429 point geometry of a branch, with their centers of mass reprojected into one of
430 the 2D images of the scene. The 2D localization errors are shown in red line
431 segments.

432 Now, we proceed to discuss the results obtained from the systematic exper-
433 iments.

434 3.2. Systematic results

435 Fig.6 reports *precision* and *recall* detection errors as well as the localization
436 error (in pixels) for all assignments obtained from the following values of the four
437 free parameters $\tau_I \in \{1, 2, 3, 4, 5\}$, $\tau_P \in \{1, 2, 3, 4\}$, $r \in \{0.01, 0.05, 0.10, 0.50, 1,$
438 $2, 3, 5, 10, 50, 100\}$, and $m \in \{1, 3, 5, 10, 25, 50, 100, 200\}$ where τ_I and τ_P are the
439 image and patch voting thresholds, respectively, and r and m are the DBSCAN

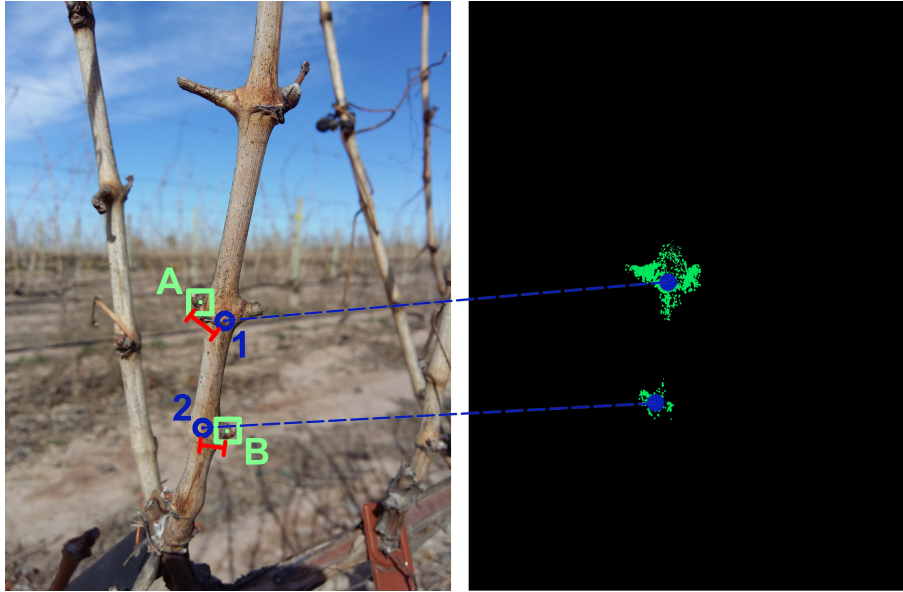


Figure 5: This figure shows the reprojection into 2D of a 3D bud detection, together with its 2D localization error, computed as the reprojection error. In the figure, the light green squares A and B (or light-gray in gray-scale version) correspond to the actual localization of the two buds, whereas the blue circles 1 and 2 (dark gray in gray-scale version) represent the reprojected center of mass. The 2D localization error of each bud is represented by the length of red line segments $1A$ and $2B$ (dark gray in gray-scale version). (For interpretation of the references to color in this figure legend, the reader is referred to the web version of the article.)

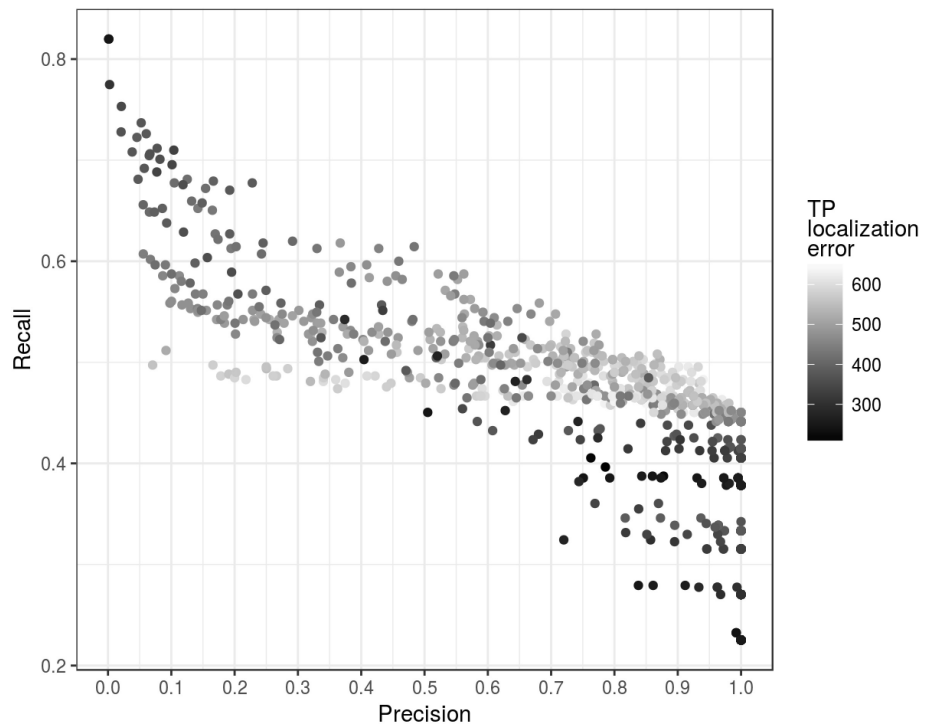


Figure 6: The figure shows recall vs precision detection errors for all assignments of the free parameters τ_I , τ_P , r , m , with a gray-scale color coding denoting the localization error in pixels (with darker color for lower errors).

440 radius and minPts, respectively. This figure shows a scatter plot of recall versus
 441 precision with a gray-scale color coding denoting the localization error. In this
 442 plot, darker colored dots represent assignments of the four free parameters with
 443 a lower localization error, with the best possible outcome for the detection error
 444 corresponding to both recall and precision equal to 1, located in the top-right
 445 corner at coordinates $(1, 1)$. Results in the plot show an abrupt fall of recall
 446 for small precisions, next, a rather constant recall after a precision of 0.2, and
 447 finally, for a large precision, a fall in recall to its lowest value of $recall = 0.2$ for
 448 $precision = 1$. The worst localization errors of approximately 600 pixels (light-
 449 gray) are concentrated at mid-range recalls of around 0.5 and decrease for either
 450 large and small recall values. As extreme assignments for the detection error,
 451 we have the upper-left case of $recall = 0.85$ and $precision \approx 0$, meaning that
 452 although most buds have been detected (85% more precisely), an extremely large
 453 number of buds has been falsely detected. On the other end, we have the dark
 454 dots in the lower right sector corresponding to $recall = 0.2$ and $precision = 1$.
 455 This case corresponds to assignments of the free parameters that incorrectly
 456 miss 80% of the buds, but on the other hand, not a single detected bud is
 457 wrong. More details of extreme assignments are shown in Table 1. Although
 458 there are no assignments close to optimal values of $(1, 1)$, it is worth highlighting
 459 that for a precision of exactly 1, recall values range between 0.22 and 0.45.

460 The data plotted in Fig.7 is the precision and recall over all assignments of
 461 the four free parameters showing two box-plots, one for precision (in light-gray)
 462 and one for recall (in dark-gray) with boxes grouping all assignments of each
 463 image voting threshold, regardless of the value of the other parameters. The
 464 figure shows a clear trend for both precision and recall, with the distribution
 465 of precision assignments leaning toward the upper values for larger thresholds,
 466 concentrating on 90% for $\tau_I = 4$, and on 100% for $\tau_I = 5$. In contrast, recall
 467 distribution moves toward lower values for large thresholds, concentrating at
 468 50% for $\tau_I = 1$ and decreasing down to 30% for $\tau_I = 5$.

Precision	Recall	#(Assignments)	Localization error of TPs	τ_I	τ_P	r	m
1	0.45	25	554.87 (34.7)	3.08	2.52	1.83	120.60
1	0.441	47	462.73 (21.98)	3.53	2.40	3.48	94.26
1	0.423	2	371.96 (2.45)	4.00	2.00	0.75	7.50
1	0.414	27	367.96 (0.0)	4.00	2.00	6.77	98.70
1	0.405	35	330.90 (0.00)	4.00	3.00	5.80	83.97
0.001	0.82	1	247.5	1.00	1.00	10.00	1.00
0.001	0.82	1	244.21	1.00	1.00	5.00	1.00
0.002	0.775	1	305.98	1.00	1.00	50.00	1.00
0.021	0.753	1	348.84	1.00	1.00	50.00	3.00
0.052	0.737	1	374.70	1.00	1.00	50.00	5.00

Table 1: A summary of best results with the top (bottom) 5 rows showing best results in terms of precision (recall). The values with the best precision (recall) are marked in bold. The column “#(Assignments)” corresponds to the number of different value assignments for the four free parameters that produced the precision and recall results of the first two columns. The table is completed with the mean and standard deviation of the true positive localization errors over these assignments and the mean of each of the four parameters over their values for each of these assignments.

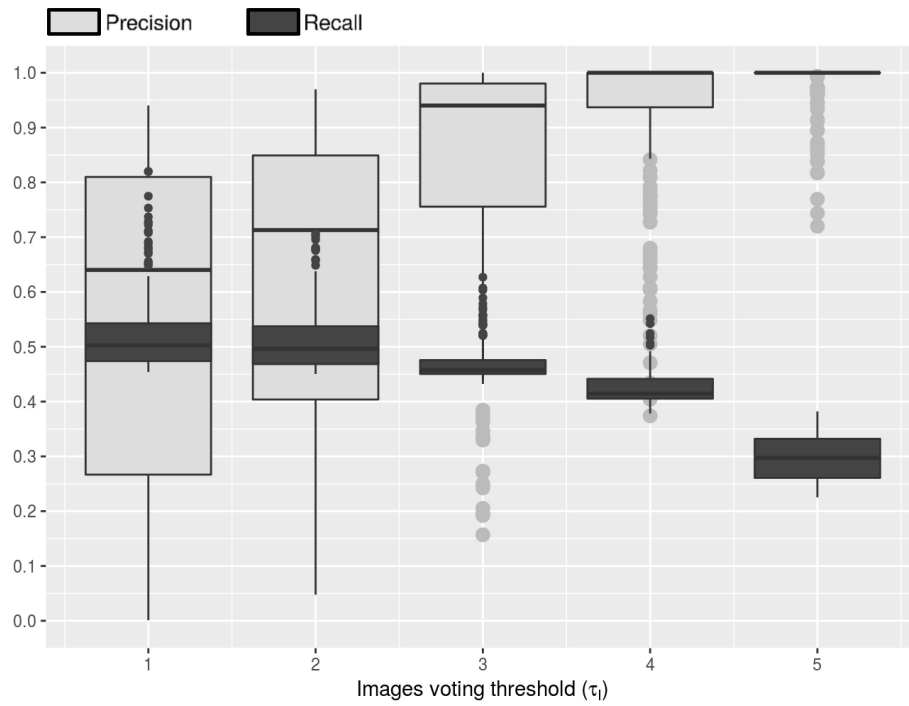


Figure 7: Trends for precision and recall. The light-gray boxes show precision and dark-gray boxes recall, with boxes grouping all assignments of the four free parameters of each voting threshold τ_l . The data plotted in the figure is precision and recall over all parameter assignments.

469 4. Discussion

470 From Fig.6 we considered as best outcomes those located at precision =
471 1 (i.e., all detections correspond to actual buds) and recall in a range from
472 0.38 to 0.45 (i.e., between 38% and 45% of buds detected). These assignments
473 show localization errors in the range of 259 – 554 pixels, which correspond to
474 approximately 3 buds and approximately 1.5cm. This is because, for the image
475 scale in the collection, average bud diameter is 159 pixels with 95% of the total
476 probability mass falling within the range of [80, 263] pixels. In the grapevine
477 variety of our study, average bud diameter is approximately 5mm.

478 We consider high precision at the expense of lower recall because we regard
479 these to be best for the central application of our work: estimation of future
480 shading (canopy) structure through simulations. As mentioned in the introduc-
481 tion, these simulation techniques take as input different numerical parameters
482 of plant architecture including, in particular, the localization of its buds. Since
483 in practice, it is an extremely difficult task to measure even the 3D localization
484 of a few buds, these simulations contemplate the possibility of localizing missing
485 buds—even all 100% of them— through stochastic procedures. In other words,
486 they contemplate low recall values, even 0%. Furthermore, these methods may
487 not easily tolerate the input of badly localized buds, or even worse, buds located
488 where in practice there is none, as it would be the case of falsely detected buds.
489 In those cases—equivalent to low precision—the simulated structure may end
490 up with false shoots, bunches, fruits and leaves. These results, however, still
491 present important limitations. First, the sampling of these 45% of buds cannot
492 be controlled or designed, but is rather biased by unknown visual characteristics
493 of the undetected buds. In addition, the workflow as presented here still depends
494 on manual capturing of a handful of images for tens of scenes per plant, a clear
495 bottleneck for high throughput. A fully automated workflow would require: (i)
496 recording all reconstructed scenes in a common coordinate system, currently
497 reconstructed into completely independent coordinate systems; (ii) automatic
498 pre-selection of images, e.g., focused, valid exposures, (iii) validation of correct

499 3D scene reconstructions, e.g., those with low reprojection errors, and (iv) au-
500 tonomous planning and positioning of an autonomous capturing device (e.g.,
501 drone) for producing valid image collections for each reconstruction.

502 While these issues render the current approach still unpractical for satisfying
503 all the requirements of the measuring process of the variables of interest, these
504 limitations may still be overcome by future research. Indeed, these results are
505 strong enough to motivate further research on the possibilities of computer
506 vision and machine learning for spatial modelling of vines. We conclude with
507 some more detail on the limitations of the two motivating applications:

- 508 • **Optimal pruning design:** Despite all the limitations, our work provides
509 agronomists with novel information on bud localization that is currently
510 almost impossible to measure. As already mentioned, this information,
511 together with a model of the plant’s architecture, can become input for
512 backward and forward simulators to improve the studies on optimal prun-
513 ing procedures. Currently, those simulators only use the plant’s architec-
514 ture, since bud localization is unavailable, while with our work they can
515 locate 45% of them with a maximum displacement of 1.5cm. Subjective
516 assessments indicate that these localization errors should not have a major
517 impact on the shading structures simulated, an assessment that can only
518 be rendered conclusive once actual simulations are performed.
- 519 • **Internode length:** This variable reports the distance between two con-
520 secutive nodes of the same branch. However, since buds always grow over
521 nodes, the distance of consecutive buds over the branch are a very close
522 approximation of internode length. On the one hand, bud localization
523 alone is insufficient, as there is no information on whether those buds be-
524 long or not to the same branch. On the other hand, integration with plant
525 architecture reconstruction techniques can easily overcome this limitation.
526 However, a 45% recall presents a more difficult challenge. This recall is
527 still too low for guaranteeing that two detected buds are indeed nearest
528 neighbors over the cane. With larger recalls, statistics may be of help by

529 reducing the probability that there is still an intermediate bud between
530 any two detected buds.

531 The trend of precision boxes Fig.7 highlights a positive feature of the work-
532 flow’s voting step: a drastic improvement in precision from 2D to 3D. As already
533 discussed above in Section 2.1, the 2D classification resulted in a precision of
534 0.0511 corresponding to 15756 non-bud patches falsely classified as bud patches.
535 Interestingly, the precision 1.0 for a voting threshold of 5 implies that none of
536 these 2D patches contributed to a 3D bud cluster. This is explained by two
537 facts: first, that larger voting thresholds require that more 2D images agree on
538 their classification of a patch for it to contribute with its keypoints in the 3D
539 cloud. Second, this helps clean up the noise by our intuition that only true bud
540 visual aspects will show in all images, while noisy aspects will tend to show in
541 only few images.

542 **5. Conclusions**

543 In this work we introduce a workflow for the localization of grapevine buds in
544 3D space obtained from plant parts 3D models reconstructed from multiple 2D
545 images, captured during the winter season, using RGB mobile phone cameras
546 in natural field conditions. The proposed workflow is based on well-known com-
547 puter vision and machine learning algorithms, such as SfM, SIFT, BoF, SVM,
548 DAISY, ORB and DBSCAN. We justified the importance of bud 3D detec-
549 tion through their potential applications, such as prolonged sunlight exposure,
550 autonomous pruning systems, and internode length. When assessed over a rep-
551 resentative range of values of user-input parameters, the best outcome obtained
552 was a precision of 1 and a recall in the range of 0.38-0.45 with a localization
553 error in the range of 259-554 pixels equivalent to approximately 3 buds. These
554 results represent an important impact of our approach to the problem of de-
555 signing optimal pruning procedures with measurement of bud sunlight exposure
556 and autonomous pruning as two relevant and challenging sub-problems. Our
557 approach has the potential of providing novel information for producing both

558 backward (previous Spring) and forward (following Spring) simulated shading
559 structures paramount for estimating sunlight exposure of buds, and with it, the
560 potential productivity of the pruning procedure. There are several automation
561 steps still missing, however, which are all addressable by future work: register-
562 ing of all the scenes in a common coordinate system, automatic pre-selection of
563 images, autonomous detection of valid scene reconstructions (e.g., low reprojec-
564 tion errors), and autonomous positioning and posing of the capturing device.
565 Finally, further research is required for improving recall, for instance, explor-
566 ing novel reconstruction techniques and novel means for aggregating 2D patch
567 classification into a detection algorithm. One could also consider integrating
568 information from other parts of the plant, for instance, following the informa-
569 tion provided by Xu et al. [38]. As discussed in Section 1.1, their work uses
570 only information about plant architecture to position buds. This information
571 is independent of that used by the workflow of our work, suggesting interesting
572 possible integrations.

573 **Acknowledgments**

574 This work was funded by the National Technological University (UTN), the
575 National Council of Scientific and Technical Research (CONICET), Argentina,
576 and the National Fund for Scientific and Technological Promotion (FONCyT),
577 Argentina. We thank the National Agricultural Technology Institute (INTA)
578 for offering their vineyards to capture the images used in this work.

579 **References**

- 580 [1] Agarwal, S., Mierle, K., 2012. Ceres solver. <http://ceres-solver.org>.
- 581 [2] Berenstein, R., Shahar, O. B., Shapiro, A., Edan, Y., 2010. Grape clusters
582 and foliage detection algorithms for autonomous selective vineyard sprayer.
583 *Intelligent Service Robotics* 3 (4), 233–243.

- 584 [3] Bradski, G., 2000. The opencv library. *Dr. Dobb's Journal: Software Tools*
585 for the Professional Programmer 25 (11), 120–123.
- 586 [4] Csurka, G., Dance, C., Fan, L., Willamowski, J., Bray, C., 2004. Visual
587 categorization with bags of keypoints. In: *Workshop on statistical learning*
588 in computer vision, ECCV. Vol. 1. Prague, pp. 1–2.
- 589 [5] Dey, D., Mummert, L., Sukthankar, R., 2012. Classification of plant struc-
590 tures from uncalibrated image sequences. In: *Applications of Computer*
591 *Vision (WACV), 2012 IEEE Workshop on. IEEE*, pp. 329–336.
- 592 [6] Diago, M.-P., Correa, C., Millán, B., Barreiro, P., Valero, C., Tardaguila,
593 J., 2012. Grapevine yield and leaf area estimation using supervised classi-
594 fication methodology on rgb images taken under field conditions. *Sensors*
595 12 (12), 16988–17006.
- 596 [7] Ester, M., Kriegel, H.-P., Sander, J., Xu, X., et al., 1996. A density-based
597 algorithm for discovering clusters in large spatial databases with noise. In:
598 *Kdd*. Vol. 96. pp. 226–231.
- 599 [8] Fu, P., Rich, P. M., 2002. A geometric solar radiation model with applica-
600 tions in agriculture and forestry. *Computers and electronics in agriculture*
601 37 (1), 25–35.
- 602 [9] Harris, C., Stephens, M., 1988. A combined corner and edge detector. In:
603 *Alvey vision conference*. Vol. 15. Manchester, UK, pp. 10–5244.
- 604 [10] Hartley, R., Zisserman, A., 2003. *Multiple View Geometry in Computer*
605 *Vision*. Cambridge books online. Cambridge University Press.
- 606 [11] Hellman, E. W., 2003. *Grapevine structure and function*. Oregon Viticul-
607 ture. Hellman, EW (Ed.). Oregon State University Press, Corvallis, 5–19.
- 608 [12] Herzog, K., et al., 2014. Initial steps for high-throughput phenotyp-
609 ing in vineyards. *Australian and New Zealand Grapegrower and Wine-*
610 *maker* (603), 54.

- 611 [13] Iandolino, A., Pearcy, R., Williams, L., 2013. Simulating three-dimensional
612 grapevine canopies and modelling their light interception characteristics.
613 Australian Journal of Grape and Wine Research 19 (3), 388–400.
- 614 [14] Keller, M., 2015. The science of grapevines: anatomy and physiology. Aca-
615 demic Press.
- 616 [15] Khanduja, S., Balasubrahmanyam, V., 1972. Fruitfulness of grape vine
617 buds. Economic Botany 26 (3), 280–294.
- 618 [16] Louarn, G., Lecoeur, J., Lebon, E., 2008. A three-dimensional statistical
619 reconstruction model of grapevine (*vitis vinifera*) simulating canopy struc-
620 ture variability within and between cultivar/training system pairs. Annals
621 of Botany 101 (8), 1167–1184.
- 622 [17] Lowe, D. G., 2004. Distinctive image features from scale-invariant key-
623 points. International journal of computer vision 60 (2), 91–110.
- 624 [18] Muja, M., Lowe, D. G., 2009. Fast approximate nearest neighbors with
625 automatic algorithm configuration. In: International Conference on Com-
626 puter Vision Theory and Application VISSAPP'09). INSTICC Press, pp.
627 331–340.
- 628 [19] Nuske, S., Achar, S., Bates, T., Narasimhan, S., Singh, S., 2011. Yield
629 estimation in vineyards by visual grape detection. In: Intelligent Robots
630 and Systems (IROS), 2011 IEEE/RSJ International Conference on. IEEE,
631 pp. 2352–2358.
- 632 [20] Pérez, D. S., Bromberg, F., Díaz, C. A., 2017. Image classification for de-
633 tection of winter grapevine buds in natural conditions using scale-invariant
634 features transform, bag of features and support vector machines. Comput-
635 ers and Electronics in Agriculture 135, 81–95.
- 636 [21] Perez, J., Kliewer, W. M., 1990. Effect of shading on bud necrosis and bud
637 fruitfulness of thompson seedless grapevines. American Journal of Enology
638 and Viticulture 41 (2), 168–175.

- 639 [22] Powers, D. M., 2011. Evaluation: from precision, recall and f-measure to
640 roc, informedness, markedness and correlation.
- 641 [23] Reynolds, A. G., Heuvel, J. E. V., 2009. Influence of grapevine training
642 systems on vine growth and fruit composition: a review. *American Journal*
643 *of Enology and Viticulture* 60 (3), 251–268.
- 644 [24] Rublee, E., Rabaud, V., Konolige, K., Bradski, G., 2011. Orb: An effi-
645 cient alternative to sift or surf. In: *Computer Vision (ICCV), 2011 IEEE*
646 *international conference on. IEEE*, pp. 2564–2571.
- 647 [25] Sánchez, L. A., Dokoozlian, N. K., 2005. Bud microclimate and fruitfulness
648 in *vitis vinifera* l. *American Journal of Enology and Viticulture* 56 (4), 319–
649 329.
- 650 [26] Schöler, F., Steinhage, V., 2011. Towards an automated 3d reconstruc-
651 tion of plant architecture. In: *International Symposium on Applications of*
652 *Graph Transformations with Industrial Relevance. Springer*, pp. 51–64.
- 653 [27] Skinkis, P., Vance, A. J., et al., 2013. Understanding vine balance: An
654 important concept in vineyard management.
- 655 [28] Snavely, N., Seitz, S. M., Szeliski, R., 2008. Modeling the world from in-
656 ternet photo collections. *International Journal of Computer Vision* 80 (2),
657 189–210.
- 658 [29] Šúri, M., Hofierka, J., 2004. A new gis-based solar radiation model and its
659 application to photovoltaic assessments. *Transactions in GIS* 8 (2), 175–
660 190.
- 661 [30] Tardaguila, J., Diago, M., Blasco, J., Millán, B., Cubero, S., García-
662 Navarrete, O., Aleixos, N., 2012. Automatic estimation of the size and
663 weight of grapevine berries by image analysis. In: *International Conference*
664 *of Agricultural Engineering. Valencia Spain. pp. 8–12.*

- 665 [31] Tardaguila, J., Diago, M., Millan, B., Blasco, J., Cubero, S., Aleixos, N.,
666 2012. Applications of computer vision techniques in viticulture to assess
667 canopy features, cluster morphology and berry size. In: I International
668 Workshop on Vineyard Mechanization and Grape and Wine Quality 978.
669 pp. 77–84.
- 670 [32] Tola, E., Lepetit, V., Fua, P., 2010. Daisy: An efficient dense descriptor
671 applied to wide-baseline stereo. *IEEE transactions on pattern analysis and*
672 *machine intelligence* 32 (5), 815–830.
- 673 [33] Triggs, B., McLauchlan, P. F., Hartley, R. I., Fitzgibbon, A. W., 1999.
674 Bundle adjustment—a modern synthesis. In: *International workshop on*
675 *vision algorithms*. Springer, pp. 298–372.
- 676 [34] Vapnik, V., 2013. *The nature of statistical learning theory*. Springer science
677 & business media.
- 678 [35] Vasconcelos, M. C., Greven, M., Winefield, C. S., Trought, M. C., Raw, V.,
679 2009. The flowering process of *vitis vinifera*: a review. *American Journal*
680 *of Enology and Viticulture* 60 (4), 411–434.
- 681 [36] Wang, X., Han, T. X., Yan, S., 2009. An hog-lbp human detector with par-
682 tial occlusion handling. In: *Computer Vision, 2009 IEEE 12th International*
683 *Conference on*. IEEE, pp. 32–39.
- 684 [37] Whalley, J., Shanmuganathan, S., 2013. Applications of image processing
685 in viticulture: A review.
- 686 [38] Xu, S., Xun, Y., Jia, T., Yang, Q., 2014. Detection method for the buds on
687 winter vines based on computer vision. In: *Computational Intelligence and*
688 *Design (ISCID), 2014 Seventh International Symposium on*. Vol. 2. IEEE,
689 pp. 44–48.